Journal of Magnetic Resonance 305 (2019) 219–231

Contents lists available at ScienceDirect

Journal of Magnetic Resonance

journal homepage: www.elsevier.com/locate/jmr

A suite of solid-state NMR experiments to utilize orphaned magnetization for assignment of proteins using parallel high and low gamma detection

A. Gallo [a,1], W.T. Franks [a,b,1], J.R. Lewandowski [a,*]

[a] Department of Chemistry, University of Warwick, Gibbet Hill Road, CV4 7AL Coventry, UK
[b] Department of Physics, University of Warwick, Gibbet Hill Road, CV4 7AL Coventry, UK

ARTICLE INFO

Article history:
Received 22 May 2019
Revised 3 July 2019
Accepted 5 July 2019
Available online 6 July 2019

Keywords:
Multiple receivers
Solid-state NMR
Protein
Discarded magnetization pathways
Low–γ
Fast magic angle spinning

ABSTRACT

We present a suite of two-receiver solid-state NMR experiments for backbone and side chain resonance assignment. The experiments rely on either dipolar coupling or scalar coupling for polarization transfer and are devised to acquire a ^{1}H–detected 3D experiment AND a nested ^{13}C–detected 2D from a shared excitation pulse. In order to compensate for the lower sensitivity of detection on ^{13}C nucleus, 2D rows are signal averaged during 3D planes. The 3D dual receiver experiments do not suffer from any appreciable signal loss compared to their single receiver versions and require no extra optimization. The resulting data is higher in information content with no additional experiment time. The approach is expected to become widespread as multiple receivers become standard for new NMR spectrometers.

1. Introduction

Solid state nuclear magnetic resonance (ssNMR) spectroscopy is a powerful method for characterizing the structure and dynamics [1–4] of a wide variety of protein preparations including microcrystals [5–10], fibrils [11–17], sediments, membrane proteins [18–21] as well as both homomeric and heteromeric assemblies [22,23]. This approach is increasingly being used to non-destructively characterize the biomolecular machinery to better understand drug activity and cellular signaling at atomic resolution, sometimes in nearly-natural conditions [19,24–28]. While NMR can provide unique data, the multidimensional experiments needed to study large biomolecules are generally slow and insensitive. In the recent years, there was a concerted effort to improve practicality and take advantage of high sensitivity of ^{1}H–detected biomolecular experiments by combatting the ^{1}H line broadening through fast spinning and/or dilution of the proton network by deuteration [23,29–36]. ^{1}H–detected experiments have proven beneficial for spectral assignment [23,37–40], structure determination [41,42], and quantification of dynamics [10,43–46]. On the other hand, the ^{13}C–detected experiments are typically not measured under conditions favorable for ^{1}H–detected experiments, i.e. fast spinning in small rotors, due to poor sensitivity caused by the reduction of the sample size and/or the removal of a large portion of the high–γ nuclei.

Several approaches to collect data more efficiently without specialized hardware have been invented over the years with the aim to both reduce the overall experimental time and to improve sensitivity and/or resolution. These data collection schemes can be generalized into four approaches: altered sampling, frequency encoded, relaxation optimized, and polarization optimized. In the first approach, altered sampling experiments, *e.g.* GFT NMR spectroscopy [47,48], Non-Uniform Sampling (NUS) [49–53] and Projection Reconstruction (PR) [54], do not sample a full, evenly-spaced rectangular grid of time points in the indirect dimensions, but rather a subset of points not necessarily tied to the rectangular grid. In the second approach, frequency encoding selectively excites either a portion of the sample by using gradients and imaging techniques (or an orientation-dependent term) as in single scan NMR [55,56] or by exciting a portion of the spectrum using selective pulses as in Hadamard NMR [57,58]. The third approach relies on relaxation optimized methods, which seek to minimize the time needed between sampling points by reducing ^{1}H T_1 and consequently the wait time between experiments either through clever spin manipulations as in BEST (Band-selective Excitation Short-Transient) and SO-FAST (band-Selective Optimized Flip-Angle

* Corresponding author.
E-mail address: J.R.Lewandowski@warwick.ac.uk (J.R. Lewandowski).
[1] Authors have contributed equally.

https://doi.org/10.1016/j.jmr.2019.07.006
1090-7807/

Short-Transient) [59–61] or addition paramagnetic dopants to the sample [62–64]. In the fourth approach, "many-at-once" experiments aim to make the most of the initial polarization by collecting more than one experiment per excitation pulse. For example, time-shared experiments allow the polarization to follow multiple pathways with two (or more) experiments being obtained during one acquisition taking advantage of either phase labelling, or chemical shift differences [65–72]. Alternatively, experiments such as DUMAS (DUal acquisition Magic Angle Spinning) [73], MAESTRO [74], MAESTOSO (Multiple Acquisitions via Sequential Transfer of Orphan Spin pOlarization) [75,76], Multiple Sequential Acquisitions [77], and UTOPIA (Unified Time-Optimized Interleaved Acquisition NMR) [78] yield multiple experiments with a small time penalty by acquiring different pathways sequentially with fraction of the magnetization being stored in a long-lived state during the encoding of the first pathway.

The frequency encoded approach is difficult to apply to biological MAS NMR; the single scan technique requires very strong, well-aligned and reproducible gradients, which are challenging for MAS probes, and there are typically no anisotropic couplings large enough for orientation selection [79,80]. In addition, the extent of inhomogeneous broadening typical for solid samples is too large for Hadamard encoding. However, the other three approaches are in current use.

Perhaps the most commonly employed approach is paramagnetic doping used with both deuterated and protonated protein samples in ^{1}H–detected [23,63,81] and ^{13}C–detected experiments [64]. Since doping also enhances transverse relaxation, this approach requires a balance between the extent of ^{1}H T_1 reduction and the overall line broadening [81]. The BEST and SO-FAST experiments rely on scalar-coupling based transfers that require ^{1}H transverse relaxation times longer than typically observed even with 100 kHz spinning and thus, currently, do not provide a competitive edge over traditional approaches except for special cases. They could, however, become more practical as yet faster spinning frequencies become available.

The second most popular method is likely non-uniform sampling (NUS) [82,83] for arbitrarily high dimensional (nD with $n \geq 3$) data. NUS is a well-supported technology with several tools available through both commercial and non-commercial software. NUS is certainly an important tool to address resolution in large systems and can be applied to a broad range of experiments.

Finally, the polarization-optimized, "many-at-once" approach is attractive due to the ability to acquire multiple experiments at the same time. Polarization that is otherwise discarded, or orphaned, after the primary polarization transfer steps, and the long longitudinal relaxation times of certain nuclei enable the acquisition of multiple experiments either simultaneously [70] or sequentially; on one or two channels [77]. Experiments with same dimensionality can be recorded using multiple receivers, in general [84], but the large difference in sensitivity between nuclei makes such a solution impractical except in special cases, *e.g.* for small, isotopically labelled molecules or when considering various quadrupolar nuclei with comparable sensitivity. In the present study, we propose a practical solution on how one can utilize multiple receivers where the sensitivity on different channels is dramatically different. Towards this end, we use an approach similar to the UTOPIA scheme [78] but with a dual receiver set-up to acquire nested lower dimensionality spectra (here, a 2D) on a secondary channel while acquiring a higher dimensionality spectrum (here a 3D) on the primary nucleus. In contrast to a standard UTOPIA approach, the lower sensitivity of the low-γ nucleus is compensated for by acquiring more transients per point for the 2D compared to the more sensitive ^{1}H–detected 3D, at the cost of an additional chemical shift dimension. Specifically, we describe a two-receiver approach to modify solid-state ^{1}H–detected 3D experiments for backbone and sidechain assignments and to simultaneously obtain ^{13}C–detected 2D spectra where the additional 2D is obtained without disturbing the 3D polarization transfer pathway. We describe a suite of experiments (available on-line at http://wrap.warwick.ac.uk/116953/) using a selection of both dipolar and scalar-coupling based carbon homonuclear mixing schemes.

The experiments presented here are designed to facilitate spectral assignment by increasing the information content with little additional setup or signal loss. The low– γ detection complements the 3D data by providing direct evidence of the polarization pathway, generating an additional 2D spectrum involving frequencies not encoded in the parent 3D under identical experimental conditions, and maximizing the resolution for the directly detected low–γ nuclei. Our approach offers certain tangible advantages over the prior art. In relation to multiple receiver experiments developed primarily by Kupce [84], the reduced dimensionality of the low–γ detected experiments allows for adequate sensitivity without lengthening the experiment time for the high– γ detected experiment. Other orphaned-polarization methods [73–77] require the full optimization of all polarization transfers for claw-back, while the experiments presented here can produce useful information once the primary HNC transfer path is established without the need for extra transfers. It may be possible to merge more "parent" and "child" experiments using the other orphaned-polarization techniques, but that is beyond the scope of this work. Finally, the UTOPIA experiments utilized one receiver, and switched it between channels, while our approach had dedicated receivers for each detect channel. It is likely that our approach is more easily implemented, and expanded upon, in state-of-the-art spectrometers, while older spectrometers must adapt the UTOPIA channel switching implementation. Neither of the two implementations are integrated into the existing "MC" macro infrastructure.

2. Materials and methods

2.1. Sample preparation

Uniformly ^{1}H/^{13}C/^{15}N labelled GB1 (T2Q mutant) was prepared as described previously [7] and doped with 4,4-dimethyl-4-silapentane-1-sulfonic acid (DSS) as an internal standard. ~0.5 mg of microcrystalline protein slurry was packed into a Bruker 0.7 mm zirconia solid-state NMR.

2.2. NMR experiments

All experiments were acquired on a Bruker Avance III spectrometer operating at 700.13 MHz ^{1}H frequency with two receivers running Topspin 3.5 patch level 6. A Bruker three channel 0.7 mm MAS probe was tuned to ^{1}H–^{13}C–^{15}N, and the sample spinning was controlled to 100 kHz ± 3 Hz. The temperature of the sample was regulated using 500 L/h gas flow with a nominal set-point of 278 K. The sample temperature is estimated to be ~300 K based on the difference between the water resonance and the DSS peak at 0.0 ppm [85,86].

Hard pulses were calibrated such that the ^{1}H 90° pulses were 2.0 μs ($\nu_{1,H}$ = 125 kHz), and both ^{13}C and ^{15}N were either 2.5 μs (ν_1 = 100 kHz) or 3.6 μs (ν_1 = 70 kHz). Low-power ($\nu_{1,H} \sim 10$ kHz) ^{1}H WALTZ-64 decoupling was applied during evolution, acquisition, and the scalar transfer periods of the heavy nuclei. Low-power ($\nu_{1,N} \sim 10$ kHz) WALTZ-64 ^{15}N decoupling was applied during ^{1}H acquisition [87]. The MISSISSIPPI (xyxy) solvent suppression scheme was used with 4 spinlock pulses of ~15 ms each and ~25 kHz spinlock, however, the homo-spoil gradient is omitted [88]. Q3 Gaussian cascade pulses with 1000 points were calibrated for selective inversion with 165 μs (bandwidth of 20.5 kHz or

~115 ppm), 320 μs (bandwidth of 10.5 kHz or ~60 ppm), and 760 μs (bandwidth of 5.3 kHz or ~30 ppm) [89]. The carbon frequency was altered by changing the spectrometer offset frequency using pre-defined constants. To avoid phase accumulation the frequency was changed either during the *Z*-filter period immediately prior to a spin-lock, or pulses were included that compensate for the phase accumulation. Each ^{1}H and ^{13}C FID was acquired for 30 ms with a spectral width of 20 ppm and 400 ppm respectively. A relaxation delay of 2 s was used for all experiments. The States-TPPI method was employed for quadrature detection in the indirect dimensions [90].

^{1}H–^{13}C cross-polarization (CP) with average $\nu_{1,H} \sim 110$ kHz and a linear 15% ramp (85%-100%, from ~101.5 to 119.5 kHz) and a zero-quantum (ZQ) match condition at $\nu_{1,C} \sim 10$ kHz was used for carbon excitation. The contact time was 350 μs and the carrier was set to 55 ppm for the initial ^{1}H–^{13}C$^{\alpha}$ CP carbon excitation, the contact time was 2 ms and the carrier was set to 40 ppm for ^{1}H–^{13}C^{ali} CP, and finally, the contact time was 2.25 ms and the carrier was set to 175 ppm for the ^{1}H–^{13}CO CP. ^{13}C–^{15}N selective transfer was optimized by 2-variable array search over a variety of possible match conditions. The optimum transfer for SPECIFIC CP [91] was observed for $\nu_{1,N} \sim 55$ kHz and $\nu_{1,C} \sim 45$ kHz (with an 81–99% tangent ramp, from 40.5 to 49.5 kHz) with no ^{1}H decoupling applied. The ^{15}N–^{1}H CP was performed with a 600 μs contact pulse with average $\nu_{1,H} \sim 85$ kHz with a linear 15% ramp (85%-100%, from ~78 to 92 kHz) and a double-quantum (DQ) match condition at $\nu_{1,N} \sim 15$ kHz. The ^{13}C–^{13}C RFDR [92] mixing was used with xy-8 phase scheme for a total of 96 rotor periods (960 μs) with no frequency changes. The ^{13}CO–^{13}C$^{\alpha}$ and ^{13}C$^{\alpha}$–^{13}CO DREAM [93] mixing used a ±10% tangent ramp with ~5 ms mixing where $\nu_{1,C}$ was optimized at ~45 kHz and the offset was set to the source frequency (CO and C$^{\alpha}$ respectively). For the ^{13}C$^{\alpha}$–^{13}C$^{\beta}$ DREAM, the carrier frequency was set to −10,000 Hz from the C$^{\alpha}$ resonance (approx. −150 ppm) to avoid the preferred ^{13}CO–^{13}C$^{\alpha}$ transfer. The DREAM transfer was 6 ms for ^{13}C$^{\alpha}$–^{13}C$^{\beta}$ transfer, and 7 ms for ^{13}CO–^{13}C$^{\alpha}$ and ^{13}C$^{\alpha}$–^{13}CO. The *J*–coupling delay τ for ^{13}CO–^{13}C$^{\alpha}$ transfer was set to 3.0 ms for the period when C$^{\alpha}$ is transverse and 3.5 ms for the period when CO is transverse, where $J^{\alpha}_{CO\text{-}C}$ is 55 Hz ($1/(4J) = 4.7$ ms). The *J*–coupling delay τ for the half-transfer between ^{13}C$^{\alpha}$–^{13}C$^{\beta}$ was set to 3.6 ms where $J^{\alpha}_{C\text{-}C\beta}$ is 35 Hz ($1/(4J) = 7.2$ ms; $1/(8J) = 3.6$ ms). For the TOCSY [94] experiments, the DIPSI-3 [95] scheme was used with a 16.3 ms mixing period. For narrow-band (aliphatic) transfer, the offset was 45 ppm, and the applied field was ~10 kHz. For broad-band (to both carbonyl and aliphatic carbons) transfer the offset was set to 175 ppm with a field of ~25 kHz.

Instructions on setting up multiple receiver experiments for Bruker instruments (Topspin 3.5pl6) can be found in the supplementary information and are also found in the header of the provided Bruker pulse sequence files. The pulse sequences can be downloaded from http://wrap.warwick.ac.uk/116953/. The raw spectra are available online at http://wrap.warwick.ac.uk/120508/.

3. Pulse sequence design

The ability to acquire high resolution ^{1}H–detected experiments has precipitated the need for triple-resonance experiments for spectral assignment. These experiments are usually based on solution NMR triple-resonance assignment protocols, but there are substantive differences in the types and mechanisms of mixing which are available in solid state NMR that will be addressed in detail in later sections. It is beyond the scope of this work to compile and modify all possible proton–detected experiments.

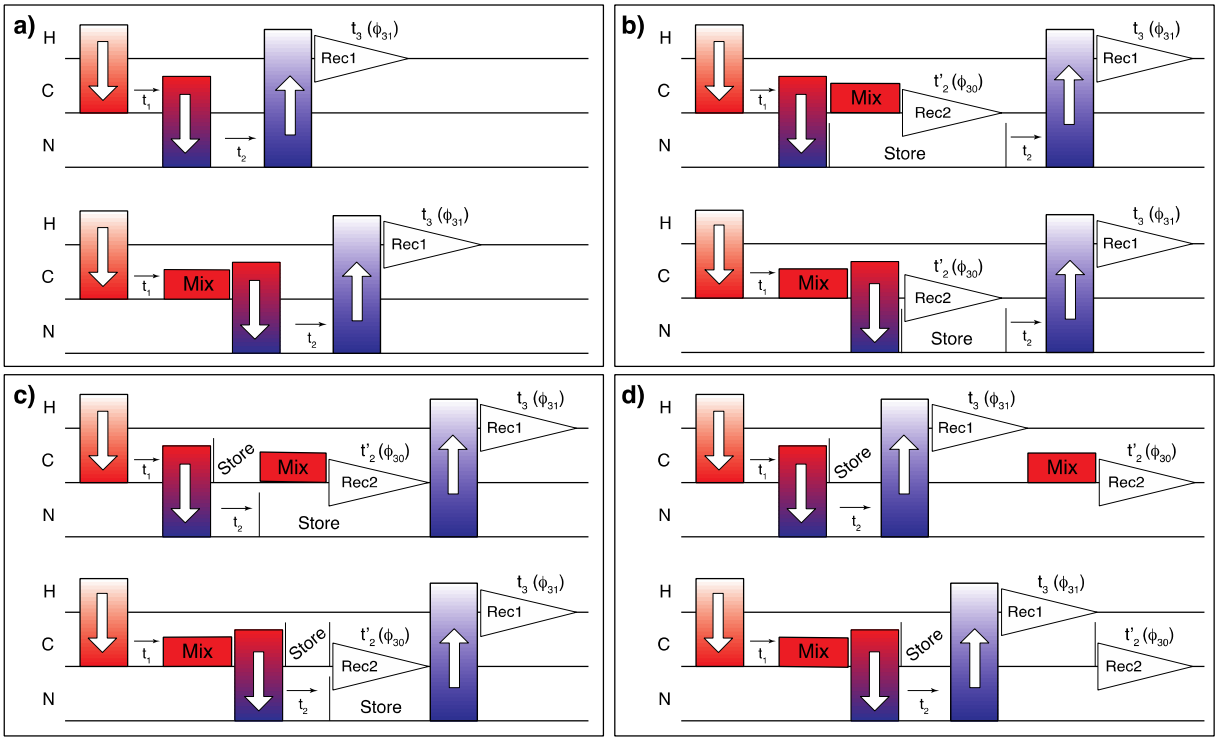

Fig. 1. Generalized pulse sequences for embedded acquisition. Panel (a) shows the polarization transfer pathway for sequential assignment commonly used with a single ^{1}H receiver. Panels (b–d) show a selection of dual receiver configurations with an added carbon detection period. The experiments yield a ^{1}H–detected 3D C(c)NH spectrum and a ^{13}C–detected CC 2D spectrum. The strategy shown in panel (b) takes advantage of long nitrogen T_1 times; this arrangement was the one preferred in this work. Configuration (c) switches the order of the nitrogen chemical shift evolution and the carbon acquisition compared to (b). Finally, in configuration (d) the orphaned carbon signal is stored until the standard 3D is finished, in order to guarantee the full preservation of the 3D sensitivity.

However, a general discussion regarding the protocol to modify 3D sequences into embedded [2D, 3D] multiple receiver experiments is warranted. To be consistent with the terminology used in the Topspin software, the higher dimensional experiment, usually acquired on the higher frequency channel (^{1}H), is referred to as the parent 3D experiment and the lower dimensional, 2D low-γ detected (^{13}C) experiment is referred to as the child.

A typical ^{1}H–detected triple-resonance backbone assignment experiments consist of a carbon excitation step (^{1}H–^{13}C CP), a ^{13}C chemical shift evolution period, possibly a carbon mixing period, followed by a ^{13}C–^{15}N transfer, an ^{15}N chemical shift evolution period, transfer from nitrogen to hydrogen (^{1}H–^{15}N CP), and finally acquisition on the ^{1}H channel (Fig. 1a). In real life applications polarization transfer is rarely >50% efficient. Some signal is left behind, or orphaned, at every transfer step during the experiment. Since we wish to observe the orphaned signal directly, an acquisition can be added after any heteronuclear transfer, while the polarization on the primary path is preserved for later. We have chosen to observe ^{13}C since it has a higher gyromagnetic ratio than ^{15}N, and it has a higher information content due to more extensive network of bonded ^{13}C nuclei. In the experiments described here, the leftover carbon signal is time and phase encoded during the 3D experiment. In order to generate 2D ^{13}C–^{13}C spectrum various carbon mixing schemes are included.

The ^{13}C acquisition period can be added in several different configurations as shown in Fig. 1b–d. The acquisition on the two receivers could take place concurrently, but doing so restricts the ability to apply decoupling, *e.g.* ^{1}H decoupling could not be applied during

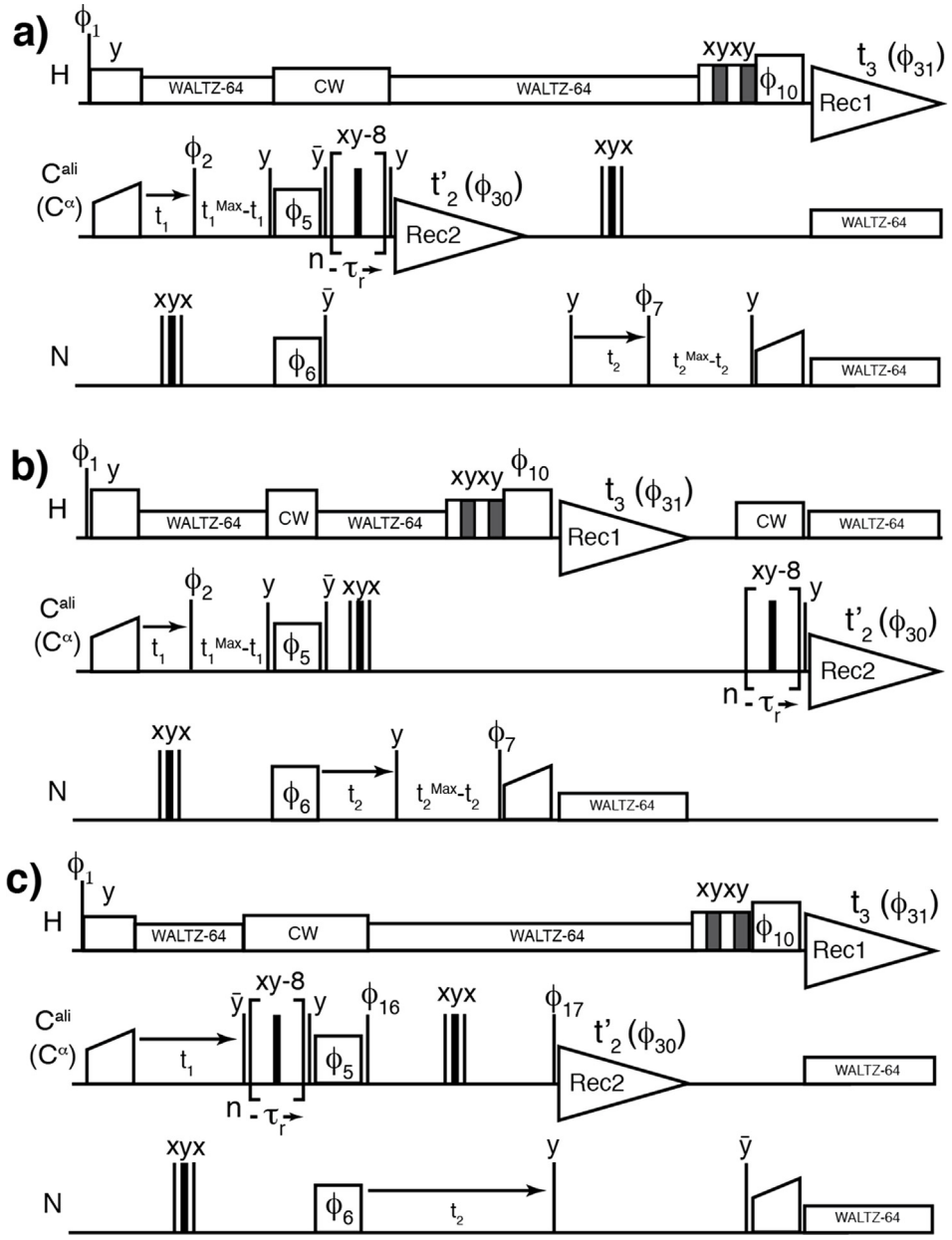

Fig. 2. Two-receiver 2D, 3D hC[C, NH] pulse sequences with longitudinal ^{13}C–^{13}C RFDR mixing. The experiments simultaneously collect a 2D (^{13}C–^{13}C) and a 3D (^{13}C–^{15}N–^{1}H) spectrum. In (a) the ^{13}C direct detection occurs between the ^{13}C–^{15}N CP step and the ^{1}H detection period. For (b) the ^{13}C detection period is moved after the ^{1}H detection to avoid any effects on the 3D. For (c), the 3D will also encode the sidechain resonance frequencies since the ^{13}C–^{13}C mixing occurs before the ^{13}C–^{15}N CP step. Narrow and broad black rectangles represent 90° and 180° hard pulses, respectively. When not shown, the phases of the pulses are x. The phase cycling is as follows: (a): ϕ_1 = (x*2, −x*2), ϕ_2 = x, ϕ_6 = (x*4, −x*4), ϕ_8 = (y, −y), ϕ_{10} = (y, y, −x, −x), ϕ_{16} = (−y, −y, y, y, −y, y, −y), ϕ_{17} = y*2, −x*2), receiver 1: ϕ_{31} = (y, −y, x, −x, −y, y, −x, x) and receiver 2: ϕ_{30} = (x, −x, −x, x, y, −y, −y, y). States-TPPI is employed on ϕ_2 for the shared ^{13}C dimension of all experiments; on ϕ_7 for (a) and (b), and ϕ_6 for (c) for the ^{15}N dimension.

^{13}C acquisition. In the configuration presented in Fig. 1b, ^{13}C acquisition is placed directly after the carbon to nitrogen CP while the nitrogen signal is stored on the Z axis; the nitrogen is frequency labelled after the carbon acquisition. This arrangement is designed to limit the signal loss from spin lattice relaxation for both pathways since the ^{15}N T_1 times are usually on the order of 10–30 s, while the ^{13}C T_1 times are typically shorter, especially for side-chain carbons. Fig. 1c shows an experiment where the order of carbon detection and nitrogen evolution is reversed from Fig. 1b. This arrangement was found to be slightly less sensitive particularly for experiments storing aliphatic carbon signal. Hence the experiments reported in this paper are primarily in the 1b configuration. Finally, the orphaned carbon signal can be stored until after the 3D is finished (Fig. 1d), so that the only alteration to the 3D is an additional short ^{13}C storage pulse after ^{13}C–^{15}N CP. This arrangement may be necessary if the homonuclear mixing and/or acquisition compromise the intensity of the 3D. In non-ideal cases, carbon-mixing schemes may also recouple the heteronuclear dipole when applied, which is detrimental to the overall 3D efficiency.

The modifications needed to adapt existing pulse sequences into an embedded multiple receiver experiment are straightforward (Fig. 1, see SI for the pulse programs in the Bruker format and instructions). The receiver phase for the embedded (child) experiment must be determined separately from the primary experiment. For example, the receiver phase of the "child" experiment is not altered by any change to the spin-lock phases during the ^{13}C–^{15}N CP, while the "parent" receiver phase must follow the changes to the spin lock phases on both channels. The phase cycling of the pulses after the ^{13}C–^{15}N CP step on the parent pathway are on an independent pathway to the "child" acquisition and cannot affect the "child" (which may have already been observed). To illustrate, in the experiment shown in Fig. 2a, changing ϕ_5 does not affect the ^{13}C receiver phase, since there is no change to the coherence order for the orphaned spins, but such a change is affected in the ^{1}H receiver. Since a 2D ^{13}C–^{13}C correlation spectrum is the desired child experiment, the ^{15}N dimension must be the inner loop. The inner (fast) loop of the 3D is used to collect one row of the child while a full plane of the parent experiment is being collected. The number of coadded transients for the child 2D is the number of transients multiplied by the number of rows in the unshared chemical shift evolution period, i.e. number of transients in 2D = (number of transients in 3D) * (number of rows = real + imaginary data in the indirect dimension), *e.g.* 16 transients * 38 TD1 = 608 transients for the child 2D. The parent data is written to disk after the specified number of scans, while the child is only written after the completion of a 3D plane (at the time of the child indirect dimension evolution; the outer loop). Such construction ensures that much larger number of transients is recorded for the ^{13}C–detected 2D child experiment compared to the 3D parent experiment thus partially compensating for the lower sensitivity of ^{13}C detection. Storage and recall pulses are added as needed.

Since the dynamics can differ greatly between proteins, and even different segments within a protein, different mixing schemes are better for different samples. Consequently, we have created and tested experiments with dipolar coupling based mixing schemes including RFDR [92] and DREAM [93] and *J*–coupling based schemes including COSY [37,38,94] and TOCSY [42]. As a general rule, dipolar transfers are better for sites with short coherence lifetimes, while scalar-coupling based schemes are better for sites with long coherence lifetimes.

4. Pulse sequences

At moderate (<20 kHz) spinning frequencies proton driven spin diffusion (PDSD) and dipolar assisted rotational recoupling (DARR) are commonly employed for longitudinal ^{13}C–^{13}C mixing. The

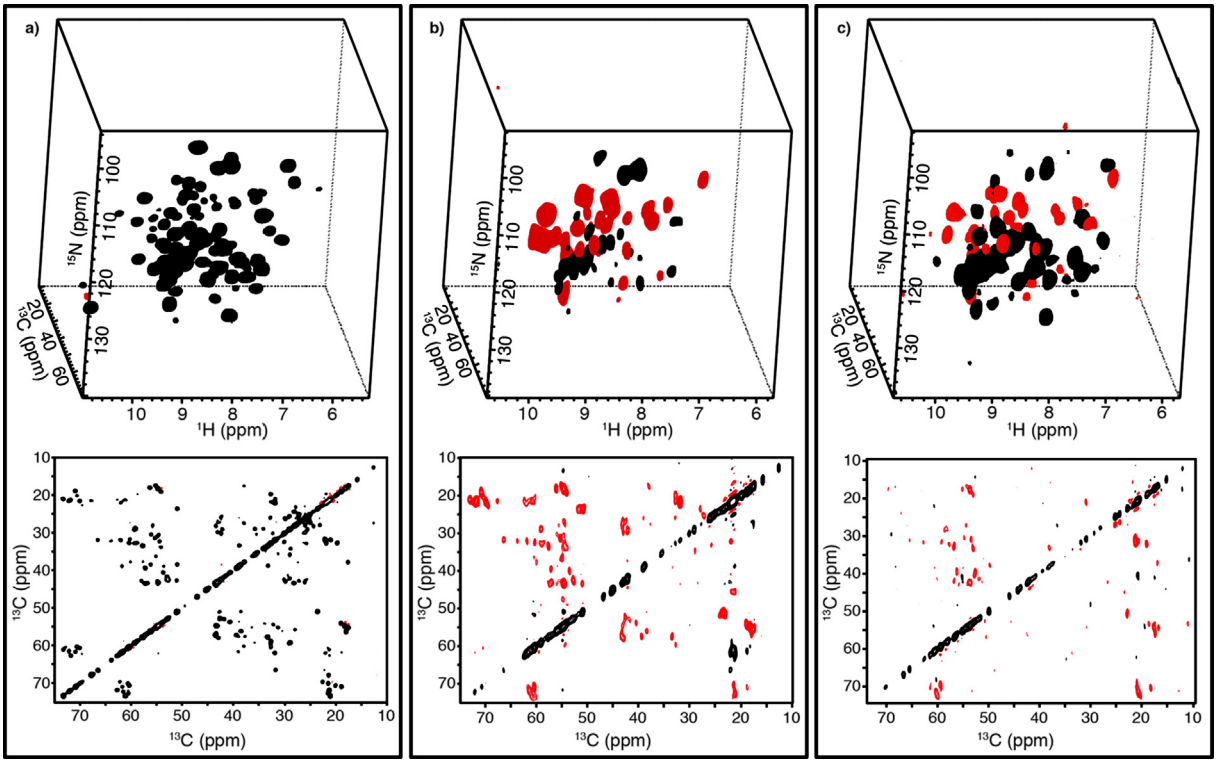

Fig. 3. Cube representation of the parent 3D $^{13}C^{\beta}/^{13}C^{\alpha}$ -^{15}N-^{1}H and child 2D $^{13}C^{\beta}$-$^{13}C^{\alpha}$ correlation spectra on crystalline [U–^{13}C, ^{15}N]GB1 acquired with (a) RFDR, (b) DREAM, and (c) COSY coupling based homonuclear ^{13}C–^{13}C mixing. Black contours are positive, and red are negative. (For interpretation of the references to colour in this figure legend, the reader is referred to the web version of this article.)

prevalence of these mixing schemes is in large part due to the easy set up rather than their superior properties. The mechanism of transfer in these experiments is deceptively complicated and is dependent on the spinning rate and magnetic field. At spinning frequencies >60 kHz and high magnetic fields proton driven spin diffusion is greatly attenuated [95] leading to poor performance for PDSD and DARR. It is thus challenging to select for one-bond ^{13}C–^{13}C polarization transfer exclusively and efficiently. Improved spin diffusion schemes for application at fast spinning frequencies have been developed but not widely adapted [96]. After spin-diffusion based ^{13}C–^{13}C longitudinal mixing, RFDR is probably the next easiest to calibrate longitudinal mixing scheme that works at very fast spinning. RFDR will be used throughout as an example of a longitudinal mixing scheme, though any other longitudinal mixing scheme can be substituted in its place in the described experiments. ^{13}C–^{13}C RFDR (and ^{13}C–^{13}C TOCSY) are better options for experiments where broad-band ^{13}C–^{13}C mixing is desirable. The DREAM and COSY schemes are more suitable for selective ^{13}C–^{13}C transfer but are typically more challenging to optimize compared to RFDR or TOCSY.

We inserted an RFDR ^{13}C–^{13}C mixing period into a 3D hCNH fingerprint experiment following the heteronuclear polarization transfer to minimize the disturbance to the 3D experiment. Fig. 2a shows a pulse sequence for a [2D, 3D] hC[C, NH] experiment where the carbon mixing and acquisition is before the nitrogen evolution, as in top of Fig. 1b (SI file war.hCA[C, NH]_RFDR_AFTER). An alternative pulse sequence (Fig. 2b) moves the ^{13}C acquisition after the 3D experiment is finished avoiding any disturbance to the 3D. The additional storage pulses are not usually phase-cycled but their presence means that a different pulse must be used for indirect dimension quadrature detection. This class of experiments (RFDR mixing) produces a 3D experiment with a series of nominally one-bond polarization transfers where a ^{13}C–^{13}C 2D is acquired at the same time, as shown in Fig. 3a. The 3D hCANH obtained on GB1 using this approach is of high quality and is comparable to the traditionally acquired single receiver experiment in terms of sensitivity and resolution. The biggest difference between the multiple receiver (hCA[C, NH]_RFDR_AFTER) and single receiver (hCANH) is that the spectral width for the indirect carbon dimension must be increased to fit the full aliphatic region instead of the CA region.

DREAM [93] can be used for transverse ^{13}C–^{13}C mixing using the pulse programs shown schematically in Fig. 4. These experiments employ a soft-hard π-pulse pair to provide frequency discrimination to ensure the correct polarization pathway is chosen during optimization, with the bonus feature that the ^{13}C–^{13}C scalar couplings are decoupled. A Z-filter is implemented before the DREAM mixing to improve the quadrature detection, provide a time for frequency switching if needed, and to ensure a constant duty cycle for the entire experiment. In this, and all following pulse schemes, we focused our effort on experiments with ^{13}C–^{13}C mixing before the ^{13}C-^{15}N transfer since these carry the

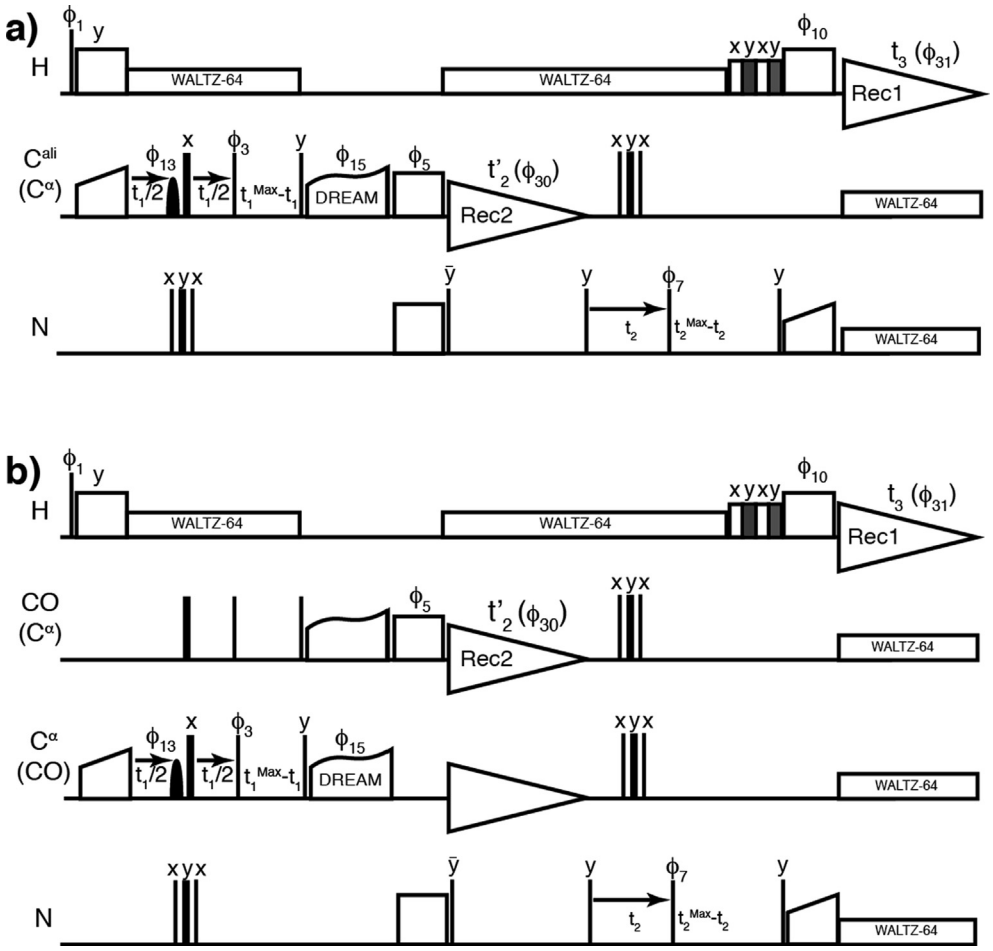

Fig. 4. Pulse sequence diagrams for [2D, 3D] assignment experiments with DREAM mixing. The 3D DREAM–based experiments for assignments results in (a) hcaCBca[C, NH] and (b) hCAco[C, NH] (hCOca[C, NH]). Rounded pulses represent 180° selective shaped pulses. Unless otherwise noted, the phase is x. For both experiments, the phase cycling is ϕ_1 = (x*2, −x*2), ϕ_3 = −y, ϕ_5 = (x*4, −x*4), ϕ_7 = y, ϕ_{10} = (y, y, −x, −x), ϕ_{13} = (x, y), ϕ_{15} = (x, −x), receiver 1 is ϕ_{31} = (−y, y, x, −x, −y, y, −x, x) and receiver 2 is ϕ_{30} = (x, −x, −x, x). States-TPPI is employed on ϕ_3 and ϕ_7. The carrier frequency is changed during the z-filter period before the DREAM period, and again between the DREAM and CP periods.

relevant backbone walk information for solution NMR-style assignments [97,98].

The h(CBCA)NH 3D with embedded 2D is shown in Fig. 3b. Because DREAM is double quantum mixing, the C^{β} peaks in the 3D, and the cross peaks of the 2D have the opposite sign of their transfer partners. This is the same as in solution NMR HNCACB experiments and can be a helpful feature during the backbone walk. In the ^{13}C–^{13}C 2D, there are positive cross-peaks in the Thr C^{α} to C γ ^{2} region, which indicates that some 2-bond, relayed transfers occurred. The digital resolution in the

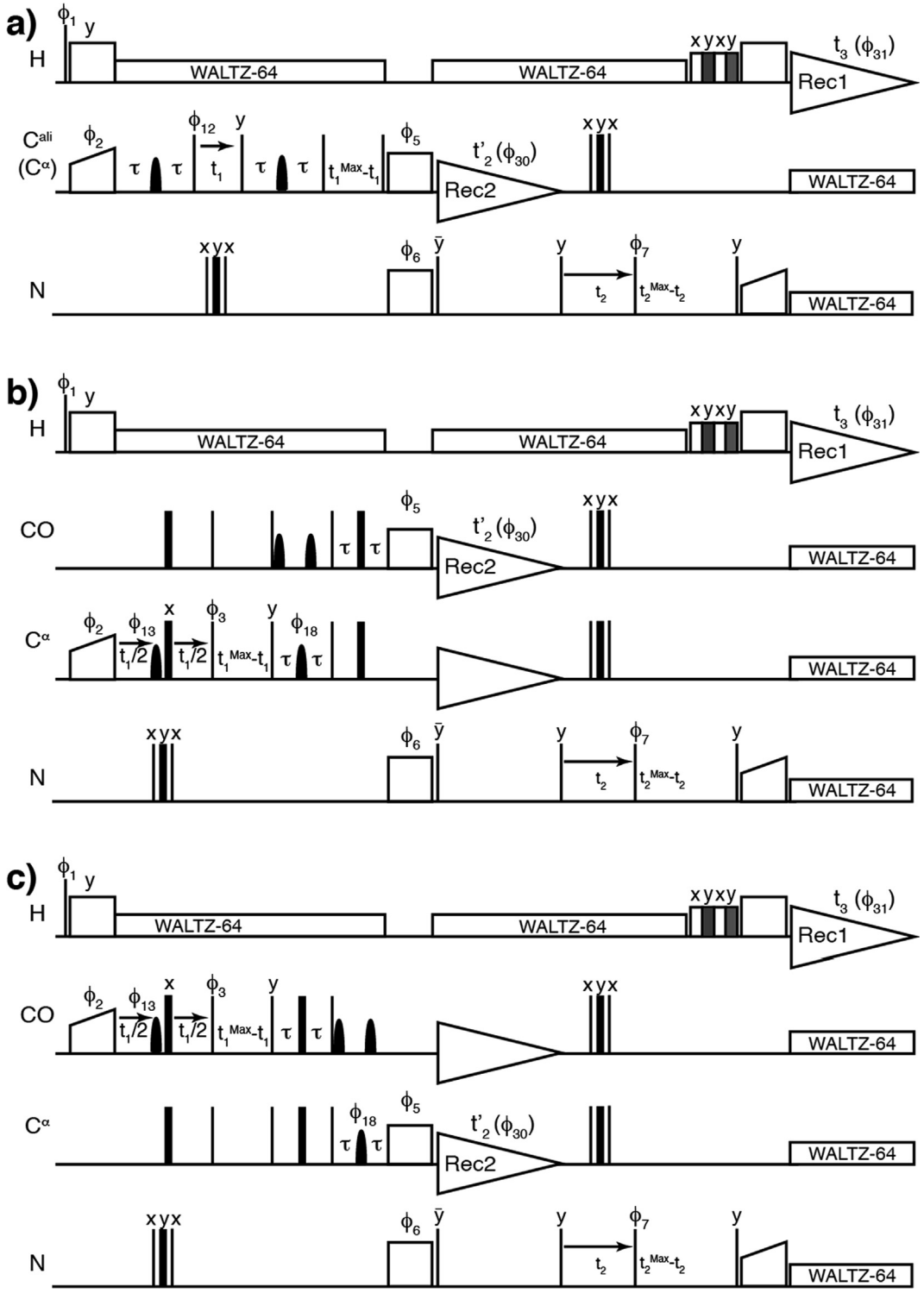

Fig. 5. Pulse sequence diagrams for [2D, 3D] assignment experiments with COSY mixing. Modifying the 3D COSY–based experiments for assignments results in (a) hcaCBca[C, NH], (b) hCAco[C, NH], and (c) hCOca[C, NH]. Rounded pulses represent 180° selective shaped pulses. Unless otherwise noted, the phase is x. For **a** the phase cycling is ϕ_0 = (y, −y), ϕ_2 = (y, y, −y, −y), ϕ_5 = (y*4, −y*4), ϕ_6 = (x*8, −x*8), ϕ_7 = −y, ϕ_{12} = y, ϕ_{13} = y, ϕ_{14} = x, receiver 1 is ϕ_{31} = (x, −x, −x, x, −x, x, x, −x, −x, x, x, −x, x, −x, −x, x) and receiver 2 is ϕ_{30} = (x, −x, −x, x). For **b** and **c** the phase cycling is ϕ_0 = y ϕ_1 = (x, −x), ϕ_3 = −y, ϕ_6 = (x*8, −x*8), ϕ_7 = y, ϕ_{13} = (x, x, y, y), ϕ_{18} = (x*4, y*4); receiver 1 is ϕ_{31} = (−y, y, y, −y, y, −y, −y, y, y, −y, −y, y, −y, y, y, −y) and receiver 2 is ϕ_{30} = (x, −x, −x, x, −x, x, x, −x). States-TPPI is employed on ϕ_2, ϕ_{12} and ϕ_7 in **a** and ϕ_3 and ϕ_7 in **b** and **c**.

indirect ^{13}C dimension was reduced for the experiment in 3b compared to 3a, which explains some of the apparent change in linewidth between the two experiments. The sample had also partially dehydrated between the collection of the datasets. In the ^{13}C–^{13}C 2D DREAM, the signals of the C^{α} nuclei are more intense than the other aliphatic carbons. This difference in signal intensity might be due to the selectivity of the DREAM mixing within the full aliphatic bandwidth, or to the reduced $T_{1\rho}$ of the sidechains during the $^{13}C^{\alpha}$–^{15}N CP, and DREAM spin locks. Still, the DREAM spectrum contains information about the sidechain contained in the 2D that is lost in the 3D dataset. The $^{13}C^{\alpha}$–^{13}CO and ^{13}CO–$^{13}C^{\alpha}$ 2D experiments are of high quality, and show a very efficient DREAM transfer, and are much less challenging to optimize compared to $^{13}C^{\beta}$–$^{13}C^{\alpha}$ transfer. The ^{13}CO–$^{13}C^{\alpha}$ and $^{13}C^{\alpha}$–^{13}CO DREAM transfer efficiencies (~50%) are higher than RFDR (~15%).

The scalar coupling based sequences, COSY (hCOcaNH, hCAcoNH, hcaCBcaNH, hcaCBcacoNH) or TOCSY (hCCaNH TOCSY, and hCCONH TOCSY), are also amenable to use with parallel acquisition. The COSY–based pulse sequences, shown in Fig. 5, utilize free precession and selective echoes to transfer the polarization via the scalar coupling through the chemical bonds, in close analogy to solution NMR experiments. TOCSY experiments are useful to identify the type of amino acid sidechain when the C^{β} resonance is not sufficient. This information is needed when there are many long chain amino acids with nearly degenerate chemical shifts. TOCSY correlations can be obtained using the DIPSI3 pulse sequence as shown in Fig. 6 [99,100].

The COSY–based sequence for backbone correlations (Fig. 5a) produced a high-quality 3D, but the ^{13}C–^{13}C 2D (Fig. 3c) had somewhat poor sensitivity. As is common practice in solution NMR, the scalar coupling was half-evolved, to produce both $^{13}C^{\alpha}$ and $^{13}C^{\beta}$ resonances (where they have opposite signs). In this case the 3D was of sufficient quality for assignments, but the ^{13}C–^{13}C 2D was not. The possible explanation for the poor quality of ^{13}C–^{13}C 2D might be sample dehydration or too long *J*–coupling evolution periods based on the typical coupling magnitudes without taking relaxation into account, or insufficient decoupling during ^{13}C detection, but the true reason for the discrepancy is not known.

The primary consideration for the application of multiple receiver experiments, apart from hardware availability, is the potential loss in sensitivity of the 3D. We find that the first row of the single receiver 3D experiment is <10% higher than when in a dual receiver configuration, as shown in Fig. 7a., but we note that there is a variance of ~3% in consecutively acquired first row experiments due to noise and water suppression. We also find that the placement of the ^{13}C acquisition is not a large factor in the 3D's sensitivity, since the 3D pathway is stored on ^{15}N, and the ^{15}N T_1 times are very long (~20 s) in GB1 (and most other solid proteins). Comparing ^{13}C sensitivity between single and double receiver configuration, as shown in Fig. 7b, we found that 50–60% of the ^{13}C intensity is depleted by ^{13}C–^{15}N transfer. The placement of the ^{13}C acquisition period effects the sensitivity in a complicated, but minor way. Despite this loss, the multiple receiver versions of the experiment still result in a more efficient use of spectrometer time since a ^{13}C–^{13}C 2D would not otherwise be acquired. There is only a very

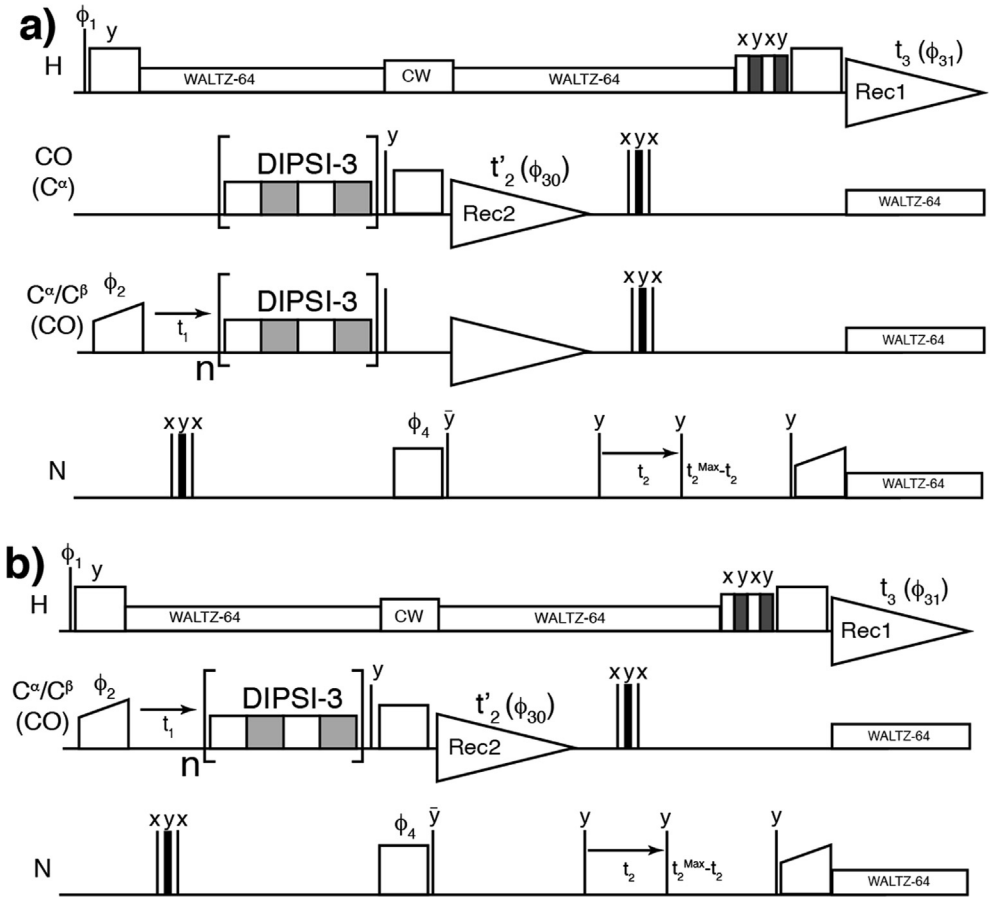

Fig. 6. Pulse sequence diagrams for [2D, 3D] assignment experiments with TOCSY mixing. 3D TOCSY experiments for (**a**) inter-residue $hC^{ali}co[C, NH]$ and (**b**) intra-residue $hC^{ali}[C, NH]$ sidechain correlations. Unless otherwise noted, the phase is x. For **a** and **b** the phase cycling is $\phi_2 = (y, y)$, $\phi_4 = (x^*4, -x^*4)$, receiver 1 is $\phi_{31} = (y, -y, x, -x, -y, y, -x, x)$ and receiver 2 is $\phi_{30} = (x, -x, -y, y, -x, x, y, -y)$. States-TPPI is employed on ϕ 2 and ϕ 4 in **a** and **b**.

small effect on the 3D spectrum intensity, and a ^{13}C–^{13}C 2D with a large number of scans is acquired for free with magnetization that would be discarded otherwise.

In summary, we use two receivers to simultaneously record complementary a ^{1}H–detected parent 3D experiment and ^{13}C–detected child 2D experiment. The ^{1}H–detected parent 3D spectra correlate ^{1}H, ^{15}N, and adjacent $^{13}CO/^{13}C^{\alpha}$-$^{13}C^{\beta}$, and aliphatic ^{13}C using a heteronuclear $^{1}H/^{13}C$, $^{15}N/^{13}C$, and finally $^{15}N/^{1}H$ cross-polarization steps, possibly with a homonuclear ^{13}C–^{13}C transfer using either an RFDR, DREAM, COSY or TOCSY schemes. The intra– and inter–residue correlations obtained in such experiments are sufficient to perform a backbone walk. A "child" 2D ^{13}C–^{13}C spectrum is acquired using a second receiver to give C^{ali}, C^{β}, C^{α} and/or CO shifts which are not observed in the parent 3D (see Figs. 8 and 9). One row in the 2D is acquired for each 3D plane, which results in a larger number of scans per point compared to 3D and thus partially offsets the lower sensitivity of ^{13}C detection compared to ^{1}H detection. The result is an efficient exploitation of the discarded ^{13}C carbon magnetization and more effective use of spectrometer time.

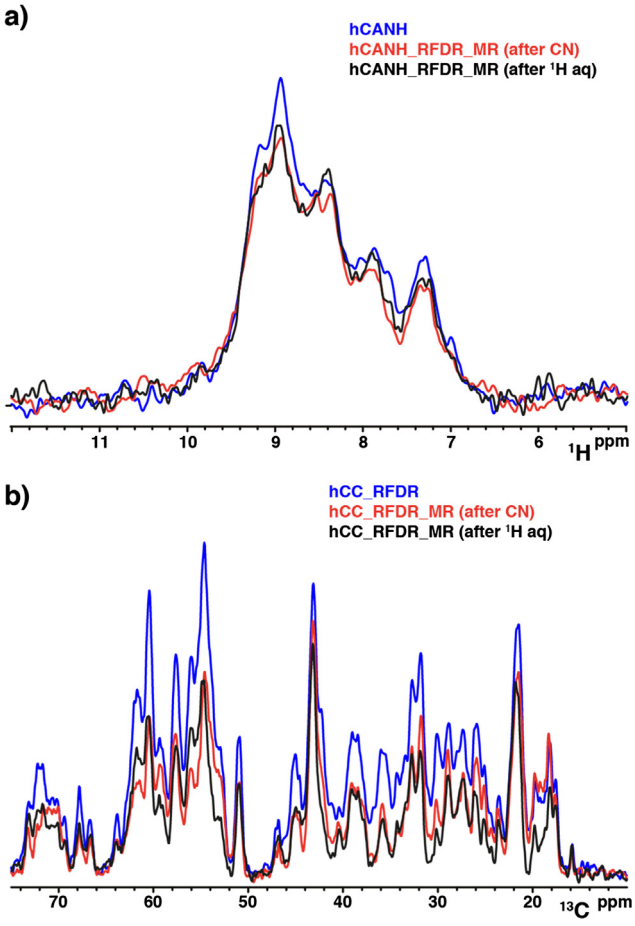

Fig. 7. Sensitivity comparison of single receiver vs dual receiver acquisition experiments. (a) 1D overlay of single receiver hCANH (blue) vs dual receiver experiments with different position of the RFDR mixing, *e.g.* RDFR after CN transfer (red) and RFDR after the 3D acquisition (black). All these experiments were acquired and processed in the same way (ns 128). (b) 1D overlay of single receiver hCC RFDR (blue) vs dual receiver experiments with different position of the RFDR mixing, *e.g.* RDFR after CN transfer (red) and RFDR after the 3D acquisition (black). All these experiments were acquired and processed in the same way. The 4864 ns is determined by the number of scans for the 3D (128) times the number of rows in the ^{15}N plane (38).

These experiments are based on the hC(c)NH polarization pathway commonly used for ^{1}H–detected assignment experiments, which is currently the best performing polarization transfer scheme for extensively deuterium labelled proteins. Any triply-labelled and back-exchanged sample that gives quality spectra should be amenable once polarization transfer conditions are found, whatever the desired spinning rate, although no such experiments were performed in this study. It should also be possible to adapt experiments that excite the initial polarization in different ways, and on all relevant nuclei [102]. While the goal of this study was to productively utilize the second receiver, it may be possible to adapt this implementation for use with one receiver, as in the UTOPIA suite of solution NMR pulse sequences. Additionally, the pulse sequences should be combatable with sparse sampling approaches, such as NUS, if care is taken such that the sampling results in the same number of scans in each row of the 2D.

However, fast spinning presents the possibility to explore alternative polarization pathways especially where there is good resolution for the sidechain protons. Out-and-stay or out-and-back schemes (hN(c)CH, hn(c)CNH) or sidechain only (hCCH) pathways should provide a way to create additional useful correlation spectra from the initial excitation. Combining multiple polarization pathways using simultaneous transfers and time-sharing with any number of sequential acquisitions on any number of receivers should be possible as shown by Gopinath and Veglia [73–75] and Sharma et al. [77].

The 3D experiments with ^{13}C–^{13}C transfer could possibly be expanded into four dimensions by adding in an evolution time for the "silent" nucleus. However, it is not clear which approach to reduce the dimensionality for the low- γ acquired spectrum is best. The most straightforward approach is to reduce the dimension by one to produce, for example, a 4D hCACONH and a 3D CACOCX. However, it might be better to utilize a separate polarization pathway to acquire a 2D (or 3D) N(co)CX. It may turn out that neither approach is tenable, and that one of the many multiple receiver experiments from solution NMR which could be adapted by applying this to approach or those designed for small molecule solution NMR, like PANACEA [84]. It should also be possible to design new experiments to measure recoupled interactions or relaxation on multiple nuclei, or to combine more experiments into this framework to improve both the data acquisition rate and to more efficiently utilize all of the initial polarization, and further development is warranted.

The resonance assignment of the micro-crystalline protein GB1 is easily confirmed from the application of the double receiver experiments (Figs. 8 and 9). While it might be unnecessary for GB1 crystals, connecting multiple nuclei to the fingerprint experiment (HN, or CC) improves confidence for the backbone assignment. The silent C^{β}, C^{α}, and CO correlations from the carbon–detected experiments essentially provide a 4th dimension of information at high resolution and should help resolve ambiguities. ^{1}H, ^{13}C, and ^{15}N resonances assignments were manually picked and interactively analyzed for all the acquired spectra. GB1 backbone cross-peaks were manually assigned corresponding to 100% of the observed backbone ^{1}H–^{15}N resonances in the CP-based ^{1}H–detected 2D ^{1}H–^{15}N correlation spectra. Full backbone and side chain assignment confirms those found in literature for 111 kHz (BMRB accession code 30088) [42].

5. Conclusion

In line with other techniques available in solution NMR, our solid-state approach relies on the parallel acquisition of several spectra using a single relaxation recycle delay. Generally, as with most multidimensional NMR experiments, the majority of the

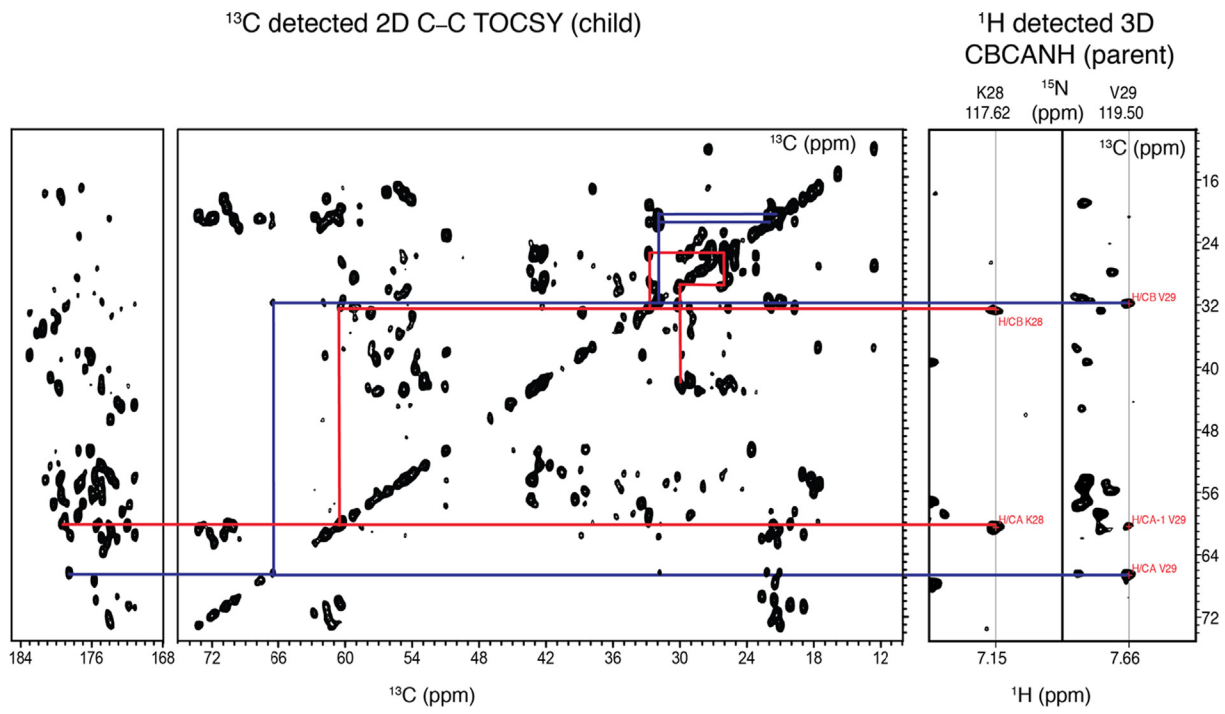

Fig. 8. Schematic representation of the intra–residue assignment process using the simultaneous and parallel acquisition. Intra-residue assignment process for the K28 (red lines) and V29 (blue lines) using the TOCSY (CBCANH 3D + C–C TOCSY 2D). (For interpretation of the references to colour in this figure legend, the reader is referred to the web version of this article.)

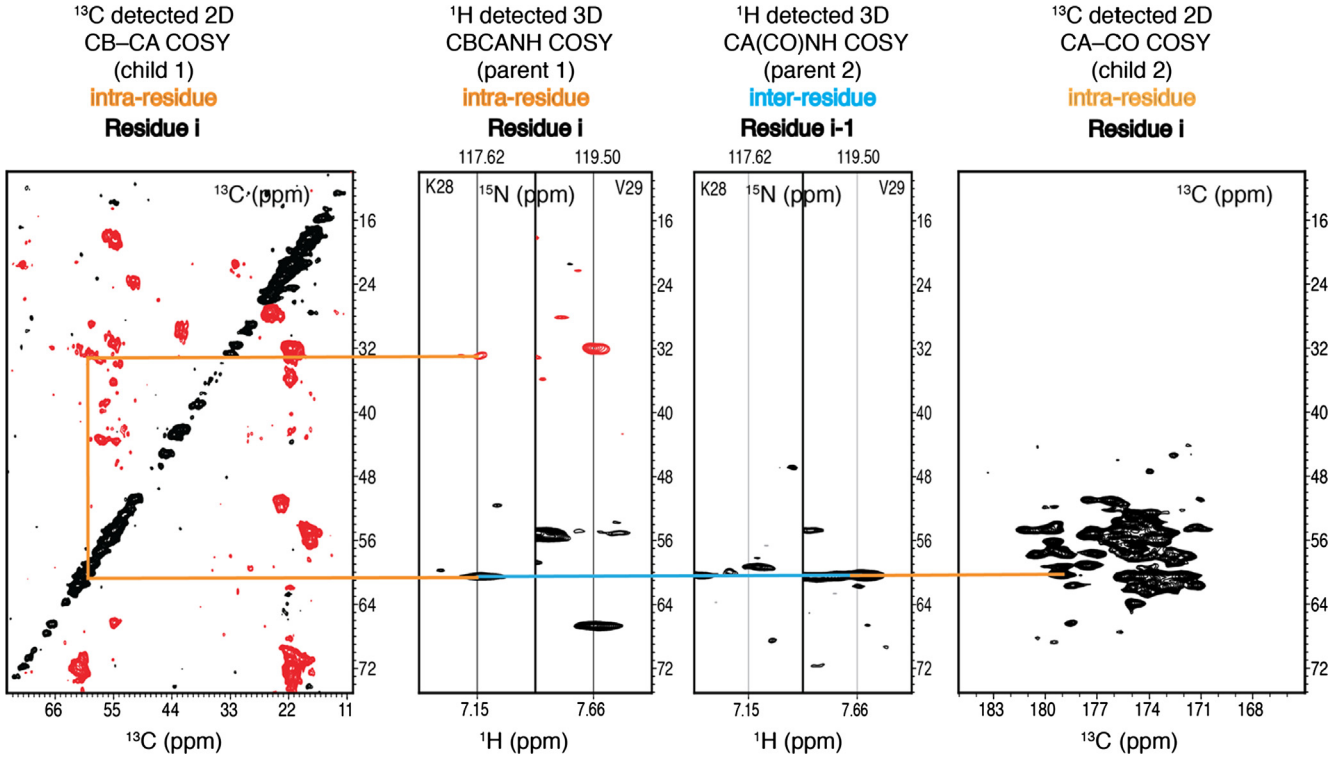

Fig. 9. Schematic representation of the intra–residue and inter–residue assignment process using the simultaneous and parallel acquisition. Intra-residue assignment process for the K28 (red lines) and V29 (blue lines) using the COSY mixing scheme. CBCANH 3D + CB–CA COSY 2D on the left (parent 1 and child 1) for the intra-residue correlations and CA(CO)NH 3D + CA–CO COSY 2D on the right (parent 2 and child 2). Positive peaks are colored in black and negative peaks are colored in red. Light orange lines indicate intra-residue correlations and blue line indicates the inter-residue correlation. (For interpretation of the references to colour in this figure legend, the reader is referred to the web version of this article.)

experimental time needed to acquire a spectrum is taken waiting for the recycle delay. It is also desirable that all available magnetization is used effectively. Indeed, in solid state NMR experiments much of the available magnetization is orphaned on the low– γ nuclei during polarization transfer. We demonstrate that the discarded magnetization from the low–γ nuclei can be effectively exploited to give useful correlation spectra. The additional low–γ acquisition can be arranged in a way that it does not compromise the efficiency of the higher dimension parent experiment, which means that the additional acquisition comes at negligible cost. Ideally such an approach provides pseudo-4D information expanding the information content of the parent 3Ds. However, the 4D may still be needed for the improved resolution that these experiments cannot wholly address. This approach could also be powerful for monitoring sample integrity in higher dimensional experiments. There is also a need to bridge a gap between datasets collected on the same biological system but on different (typically larger volume and slower spinning) MAS probes, where ^{13}C is the preferred acquisition nucleus. Additionally, portions of the protein may be incompatible with proton spectroscopy, perhaps there is motional averaging or PRE-broadening which more strongly effect the proton experiments but are not as detrimental to carbon detection [101,102].

Thus far, there have been few applications for multiple receiver spectrometers, and most have not become widespread. All Bruker spectrometers moving forward will have a receiver for each channel as standard equipment. Our approach suggests one practical way to exploit this new norm for hardware. The experiments presented here are applicable at slower MAS for substantially deuterated systems (*e.g.* 3.2 mm rotors with 20% back exchanged ^{1}H; samples produced for ^{1}H detection) given appropriate CP transfers are accessible. The modifications to the pulse sequence do not negatively affect the quality of the final spectrum in this approach, nor do they significantly increase the difficulty of the experimental optimizations, and thus we expect wide adoption.

Acknowledgements

The research leading to these results has received funding from the European Research Council under the European Union's Seventh Framework Programme (FP/2007-2013)/ERC Grant Agreement 639907. J.R.L. also acknowledges funding from BBSRC Grants BB/L022761/1 and BB/R010218/1. We also thank Dr Peter Gierth (Bruker UK) for helping in setting up the double receiver and Jacqueline Tognetti for reading the manuscript.

Appendix A. Supplementary data

Supplementary data to this article can be found online at https://doi.org/10.1016/j.jmr.2019.07.006.

References

[1] J.R. Lewandowski, Advances in solid-state relaxation methodology for probing site-specific protein dynamics, Acc. Chem. Res. 46 (2013) 2018–2027.
[2] V.S. Mandala, J.K. Williams, M. Hong, Structure and dynamics of membrane proteins from solid-state NMR, Annu. Rev. Biophys. 47 (2018) 201–222.
[3] P. Schanda, M. Ernst, Studying dynamics by magic-angle spinning solid-state NMR spectroscopy: principles and applications to biomolecules, Prog. Nucl. Magn. Reson. Spectrosc. 96 (2016) 1–46.
[4] P.C.A. van der Wel, New applications of solid-state NMR in structural biology, Emerg. Top. Life Sci. 2 (2018) 57–67.
[5] F. Castellani, B. van Rossum, A. Diehl, M. Schubert, K. Rehbein, H. Oschkinat, Structure of a protein determined by solid-state magic-angle-spinning NMR spectroscopy, Nature 420 (2002) 98–102.
[6] S.G. Zech, A.J. Wand, A.E. McDermott, Protein structure determination by high-resolution solid-state NMR spectroscopy: application to microcrystalline ubiquitin, J. Am. Chem. Soc. 127 (2005) 8618–8626.
[7] W.T. Franks, D.H. Zhou, B.J. Wylie, B.G. Money, D.T. Graesser, H.L. Frericks, G. Sahota, C.M. Rienstra, Magic-angle spinning solid-state NMR spectroscopy of the beta1 immunoglobulin binding domain of protein G (GB1): 15N and 13C chemical shift assignments and conformational analysis, J. Am. Chem. Soc. 127 (2005) 12291–12305.
[8] W.T. Franks, B.J. Wylie, H.L. Schmidt, A.J. Nieuwkoop, R.M. Mayrhofer, G.J. Shah, D.T. Graesser, C.M. Rienstra, Dipole tensor-based atomic-resolution structure determination of a nanocrystalline protein by solid-state NMR, Proc. Natl. Acad. Sci. U. S. A. 105 (2008) 4621–4626.
[9] I. Bertini, A. Bhaumik, G. De Paepe, R.G. Griffin, M. Lelli, J.R. Lewandowski, C. Luchinat, High-resolution solid-state NMR structure of a 17.6 kDa protein, J. Am. Chem. Soc. 132 (2010) 1032–1040.
[10] M.J. Knight, A.J. Pell, I. Bertini, I.C. Felli, L. Gonnelli, R. Pierattelli, T. Herrmann, L. Emsley, G. Pintacuda, Structure and backbone dynamics of a microcrystalline metalloprotein by solid-state NMR, Proc. Natl. Acad. Sci. U. S. A. 109 (2012) 11095–11100.
[11] C. Wasmer, A. Lange, H. Van Melckebeke, A.B. Siemer, R. Riek, B.H. Meier, Amyloid fibrils of the HET-s(218–289) prion form a beta solenoid with a triangular hydrophobic core, Science 319 (2008) 1523–1526.
[12] M.D. Tuttle, G. Comellas, A.J. Nieuwkoop, D.J. Covell, D.A. Berthold, K.D. Kloepper, J.M. Courtney, J.K. Kim, A.M. Barclay, A. Kendall, W. Wan, G. Stubbs, C.D. Schwieters, V.M. Lee, J.M. George, C.M. Rienstra, Solid-state NMR structure of a pathogenic fibril of full-length human alpha-synuclein, Nat. Struct. Mol. Biol. 23 (2016) 409–415.
[13] M.T. Colvin, R. Silvers, Q.Z. Ni, T.V. Can, I. Sergeyev, M. Rosay, K.J. Donovan, B. Michael, J. Wall, S. Linse, R.G. Griffin, Atomic resolution structure of monomorphic Abeta42 amyloid fibrils, J. Am. Chem. Soc. 138 (2016) 9663–9674.
[14] Y. Xiao, B. Ma, D. McElheny, S. Parthasarathy, F. Long, M. Hoshi, R. Nussinov, Y. Ishii, Abeta(1–42) fibril structure illuminates self-recognition and replication of amyloid in Alzheimer's disease, Nat. Struct. Mol. Biol. 22 (2015) 499–505.
[15] M.A. Walti, F. Ravotti, H. Arai, C.G. Glabe, J.S. Wall, A. Bockmann, P. Guntert, B. H. Meier, R. Riek, Atomic-resolution structure of a disease-relevant Abeta(1–42) amyloid fibril, Proc. Natl. Acad. Sci. U. S. A. 113 (2016) E4976–E4984.
[16] C.L. Hoop, H.K. Lin, K. Kar, G. Magyarfalvi, J.M. Lamley, J.C. Boatz, A. Mandal, J. R. Lewandowski, R. Wetzel, P.C. van der Wel, Huntingtin exon 1 fibrils feature an interdigitated beta-hairpin-based polyglutamine core, Proc. Natl. Acad. Sci. U. S. A. 113 (2016) 1546–1551.
[17] J.J. Helmus, K. Surewicz, W.K. Surewicz, C.P. Jaroniec, Conformational flexibility of Y145Stop human prion protein amyloid fibrils probed by solid-state nuclear magnetic resonance spectroscopy, J. Am. Chem. Soc. 132 (2010) 2393–2403.
[18] S.H. Park, B.B. Das, F. Casagrande, Y. Tian, H.J. Nothnagel, M. Chu, H. Kiefer, K. Maier, A.A. De Angelis, F.M. Marassi, S.J. Opella, Structure of the chemokine receptor CXCR1 in phospholipid bilayers, Nature 491 (2012) 779–783.
[19] J.S. Retel, A.J. Nieuwkoop, M. Hiller, V.A. Higman, E. Barbet-Massin, J. Stanek, L.B. Andreas, W.T. Franks, B.J. van Rossum, K.R. Vinothkumar, L. Handel, G.G. de Palma, B. Bardiaux, G. Pintacuda, L. Emsley, W. Kuhlbrandt, H. Oschkinat, Structure of outer membrane protein G in lipid bilayers, Nat. Commun. 8 (2017) 2073.
[20] B. Bersch, J.M. Dorr, A. Hessel, J.A. Killian, P. Schanda, Proton-detected solid-state NMR spectroscopy of a zinc diffusion facilitator protein in native nanodiscs, Angew. Chem. Int. Ed. Engl. 56 (2017) 2508–2512.
[21] D. Good, C. Pham, J. Jagas, J.R. Lewandowski, V. Ladizhansky, Solid-state NMR provides evidence for small-amplitude slow domain motions in a multispanning transmembrane alpha-helical protein, J. Am. Chem. Soc. 139 (2017) 9246–9258.
[22] A. Loquet, N.G. Sgourakis, R. Gupta, K. Giller, D. Riedel, C. Goosmann, C. Griesinger, M. Kolbe, D. Baker, S. Becker, A. Lange, Atomic model of the type III secretion system needle, Nature 486 (2012) 276–279.
[23] J.M. Lamley, D. Iuga, C. Oster, H.J. Sass, M. Rogowski, A. Oss, J. Past, A. Reinhold, S. Grzesiek, A. Samoson, J.R. Lewandowski, Solid-state NMR of a protein in a precipitated complex with a full-length antibody, J. Am. Chem. Soc. 136 (2014) 16800–16806.
[24] L. Krabben, B.J. van Rossum, S. Jehle, E. Bocharov, E.N. Lyukmanova, A.A. Schulga, A. Arseniev, F. Hucho, H. Oschkinat, Loop 3 of short neurotoxin II is an additional interaction site with membrane-bound nicotinic acetylcholine receptor as detected by solid-state NMR spectroscopy, J. Mol. Biol. 390 (2009) 662–671.
[25] A.H. Linden, S. Lange, W.T. Franks, U. Akbey, E. Specker, B.J. van Rossum, H. Oschkinat, Neurotoxin II bound to acetylcholine receptors in native membranes studied by dynamic nuclear polarization NMR, J. Am. Chem. Soc. 133 (2011) 19266–19269.
[26] T. Jacso, W.T. Franks, H. Rose, U. Fink, J. Broecker, S. Keller, H. Oschkinat, B. Reif, Characterization of membrane proteins in isolated native cellular membranes by dynamic nuclear polarization solid-state NMR spectroscopy without purification and reconstitution, Angew. Chem. Int. Ed. Engl. 51 (2012) 432–435.
[27] M. Renault, R. Tommassen-van Boxtel, M.P. Bos, J.A. Post, J. Tommassen, M. Baldus, Cellular solid-state nuclear magnetic resonance spectroscopy, Proc. Natl. Acad. Sci. U. S. A. 109 (2012) 4863–4868.
[28] H.L. Frericks, D.H. Zhou, L.L. Yap, R.B. Gennis, C.M. Rienstra, Magic-angle spinning solid-state NMR of a 144 kDa membrane protein complex: E. coli cytochrome bo3 oxidase, J. Biomol. NMR 36 (2006) 55–71.

[29] B. Reif, C.P. Jaroniec, C.M. Rienstra, M. Hohwy, R.G. Griffin, 1H–1H MAS correlation spectroscopy and distance measurements in a deuterated peptide, J. Magn. Reson. 151 (2001) 320–327.
[30] U. Sternberg, R. Witter, I. Kuprov, J.M. Lamley, A. Oss, J.R. Lewandowski, A. Samoson, (1)H line width dependence on MAS speed in solid state NMR – comparison of experiment and simulation, J. Magn. Reson. 291 (2018) 32–39.
[31] D.H. Zhou, D.T. Graesser, W.T. Franks, C.M. Rienstra, Sensitivity and resolution in proton solid-state NMR at intermediate deuteration levels: quantitative linewidth characterization and applications to correlation spectroscopy, J. Magn. Reson. 178 (2006) 297–307.
[32] J.R. Lewandowski, J.-N. Dumez, Ü. Akbey, S. Lange, L. Emsley, H. Oschkinat, Enhanced resolution and coherence lifetimes in the solid-state NMR spectroscopy of perdeuterated proteins under ultrafast magic-angle spinning, J. Phys. Chem. Lett. 2 (2011) 2205–2211.
[33] A. Samoson, T. Tuherm, J. Past, A. Reinhold, T. Anupold, I. Heinmaa, New horizons for magic-angle spinning NMR, Top. Curr. Chem. 246 (2005) 15–31.
[34] V. Chevelkov, B.J. van Rossum, F. Castellani, K. Rehbein, A. Diehl, M. Hohwy, S. Steuernagel, F. Engelke, H. Oschkinat, B. Reif, 1H detection in MAS solid-state NMR spectroscopy of biomacromolecules employing pulsed field gradients for residual solvent suppression, J. Am. Chem. Soc. 125 (2003) 7788–7789.
[35] A.J. Nieuwkoop, W.T. Franks, K. Rehbein, A. Diehl, U. Akbey, F. Engelke, L. Emsley, G. Pintacuda, H. Oschkinat, Sensitivity and resolution of proton detected spectra of a deuterated protein at 40 and 60 kHz magic-angle-spinning, J. Biomol. NMR 61 (2015) 161–171.
[36] J. Stanek, L.B. Andreas, K. Jaudzems, D. Cala, D. Lalli, A. Bertarello, T. Schubeis, I. Akopjana, S. Kotelovica, K. Tars, A. Pica, S. Leone, D. Picone, Z.Q. Xu, N.E. Dixon, D. Martinez, M. Berbon, N. El Mammeri, A. Noubhani, S. Saupe, B. Habenstein, A. Loquet, G. Pintacuda, NMR spectroscopic assignment of backbone and side-chain protons in fully protonated proteins: microcrystals, sedimented assemblies, and amyloid fibrils, Angew. Chem. Int. Ed. Engl. 55 (2016) 15504–15509.
[37] M.J. Knight, A.L. Webber, A.J. Pell, P. Guerry, E. Barbet-Massin, I. Bertini, I.C. Felli, L. Gonnelli, R. Pierattelli, L. Emsley, A. Lesage, T. Herrmann, G. Pintacuda, Fast resonance assignment and fold determination of human superoxide dismutase by high-resolution proton-detected solid-state MAS NMR spectroscopy, Angew. Chem. Int. Ed. Engl. 50 (2011) 11697–11701.
[38] E. Barbet-Massin, A.J. Pell, J.S. Retel, L.B. Andreas, K. Jaudzems, W.T. Franks, A. J. Nieuwkoop, M. Hiller, V. Higman, P. Guerry, A. Bertarello, M.J. Knight, M. Felletti, T. Le Marchand, S. Kotelovica, I. Akopjana, K. Tars, M. Stoppini, V. Bellotti, M. Bolognesi, S. Ricagno, J.J. Chou, R.G. Griffin, H. Oschkinat, A. Lesage, L. Emsley, T. Herrmann, G. Pintacuda, Rapid proton-detected NMR assignment for proteins with fast magic angle spinning, J. Am. Chem. Soc. 136 (2014) 12489–12497.
[39] P. Fricke, V. Chevelkov, M. Zinke, K. Giller, S. Becker, A. Lange, Backbone assignment of perdeuterated proteins by solid-state NMR using proton detection and ultrafast magic-angle spinning, Nat. Protoc. 12 (2017) 764–782.
[40] C. Oster, G.P. Walkowiak, D.E. Hughes, A.L. Spoering, A.J. Peoples, A.C. Catherwood, J.A. Tod, A.J. Lloyd, T. Herrmann, K. Lewis, C.G. Dowson, J.R. Lewandowski, Structural studies suggest aggregation as one of the modes of action for teixobactin, Chem. Sci. 9 (2018) 8850–8859.
[41] D.H. Zhou, J.J. Shea, A.J. Nieuwkoop, W.T. Franks, B.J. Wylie, C. Mullen, D. Sandoz, C.M. Rienstra, Solid-state protein-structure determination with proton-detected triple-resonance 3D magic-angle-spinning NMR spectroscopy, Angew. Chem. Int. Ed. Engl. 46 (2007) 8380–8383.
[42] L.B. Andreas, K. Jaudzems, J. Stanek, D. Lalli, A. Bertarello, T. Le Marchand, D. Cala-De Paepe, S. Kotelovica, I. Akopjana, B. Knott, S. Wegner, F. Engelke, A. Lesage, L. Emsley, K. Tars, T. Herrmann, G. Pintacuda, Structure of fully protonated proteins by proton-detected magic-angle spinning NMR, Proc. Natl. Acad. Sci. U. S. A. 113 (2016) 9187–9192.
[43] J.M. Lamley, C. Oster, R.A. Stevens, J.R. Lewandowski, Intermolecular interactions and protein dynamics by solid-state NMR spectroscopy, Angew. Chem. Int. Ed. Engl. 54 (2015) 15374–15378.
[44] V. Kurauskas, S.A. Izmailov, O.N. Rogacheva, A. Hessel, I. Ayala, J. Woodhouse, A. Shilova, Y. Xue, T. Yuwen, N. Coquelle, J.P. Colletier, N.R. Skrynnikov, P. Schanda, Slow conformational exchange and overall rocking motion in ubiquitin protein crystals, Nat. Commun. 8 (2017) 145.
[45] P. Ma, J.D. Haller, J. Zajakala, P. Macek, A.C. Sivertsen, D. Willbold, J. Boisbouvier, P. Schanda, Probing transient conformational states of proteins by solid-state R(1rho) relaxation-dispersion NMR spectroscopy, Angew. Chem. Int. Ed. Engl. 53 (2014) 4312–4317.
[46] P. Rovo, R. Linser, Microsecond timescale protein dynamics: a combined solid-state NMR approach, ChemPhysChem 19 (2018) 34–39.
[47] S. Kim, T. Szyperski, GFT NMR, a new approach to rapidly obtain precise high-dimensional NMR spectral information, J. Am. Chem. Soc. 125 (2003) 1385–1393.
[48] W.T. Franks, H.S. Atreya, T. Szyperski, C.M. Rienstra, GFT projection NMR spectroscopy for proteins in the solid state, J. Biomol. NMR 48 (2010) 213–223.
[49] P. Schmieder, A.S. Stern, G. Wagner, J.C. Hoch, Improved resolution in triple-resonance spectra by nonlinear sampling in the constant-time domain, J. Biomol. NMR 4 (1994) 483–490.
[50] V. Jaravine, I. Ibraghimov, V.Y. Orekhov, Removal of a time barrier for high-resolution multidimensional NMR spectroscopy, Nat. Methods 3 (2006) 605–607.
[51] S.G. Hyberts, K. Takeuchi, G. Wagner, Poisson-gap sampling and forward maximum entropy reconstruction for enhancing the resolution and sensitivity of protein NMR data, J. Am. Chem. Soc. 132 (2010) 2145–2147.
[52] V.Y. Orekhov, V.A. Jaravine, Analysis of non-uniformly sampled spectra with multi-dimensional decomposition, Prog. Nucl. Magn. Reson. Spectrosc. 59 (2011) 271–292.
[53] K. Kazimierczuk, V. Orekhov, Non-uniform sampling: post-Fourier era of NMR data collection and processing, Magn. Reson. Chem. 53 (2015) 921–926.
[54] E. Kupce, R. Freeman, Projection-reconstruction technique for speeding up multidimensional NMR spectroscopy, J. Am. Chem. Soc. 126 (2004) 6429–6440.
[55] L. Frydman, J. Peng, Non-Cartesian sampling schemes and the acquisition of 2D NMR correlation spectra from single-scan experiments, Chem. Phys. Lett. 222 (1994) 371–377.
[56] L. Frydman, T. Scherf, A. Lupulescu, The acquisition of multidimensional NMR spectra within a single scan, Proc. Natl. Acad. Sci. U. S. A. 99 (2002) 15858–15862.
[57] E. Kupce, R. Freeman, Fast multi-dimensional Hadamard spectroscopy, J. Magn. Reson. 163 (2003) 56–63.
[58] E. Kupce, R. Freeman, Two-dimensional Hadamard spectroscopy, J. Magn. Reson. 162 (2003) 300–310.
[59] K. Pervushin, B. Vogeli, A. Eletsky, Longitudinal (1)H relaxation optimization in TROSY NMR spectroscopy, J. Am. Chem. Soc. 124 (2002) 12898–12902.
[60] P. Schanda, B. Brutscher, Very fast two-dimensional NMR spectroscopy for real-time investigation of dynamic events in proteins on the time scale of seconds, J. Am. Chem. Soc. 127 (2005) 8014–8015.
[61] P. Schanda, H. Van Melckebeke, B. Brutscher, Speeding up three-dimensional protein NMR experiments to a few minutes, J. Am. Chem. Soc. 128 (2006) 9042–9043.
[62] S. Ganapathy, A. Naito, C.A. McDowell, Paramagnetic doping as an aid in obtaining high-resolution carbon-13 NMR spectra of biomolecules in the solid state, J. Am. Chem. Soc. 103 (1981) 6011–6015.
[63] R. Linser, V. Chevelkov, A. Diehl, B. Reif, Sensitivity enhancement using paramagnetic relaxation in MAS solid-state NMR of perdeuterated proteins, J. Magn. Reson. 189 (2007) 209–216.
[64] N.P. Wickramasinghe, M. Kotecha, A. Samoson, J. Past, Y. Ishii, Sensitivity enhancement in (13)C solid-state NMR of protein microcrystals by use of paramagnetic metal ions for optimizing (1)H T(1) relaxation, J. Magn. Reson. 184 (2007) 350–356.
[65] O. Sørensen, Aspects and prospects of multidimensional time-domain spectroscopy, J. Magn. Reson. 89 (1990) (1969) 210–216.
[66] R. Boelens, M. Burgering, R.H. Fogh, R. Kaptein, Time-saving methods for heteronuclear multidimensional NMR of ((13)C, (15)N) doubly labeled proteins, J. Biomol. NMR 4 (1994) 201–213.
[67] D.P. Frueh, H. Arthanari, G. Wagner, Unambiguous assignment of NMR protein backbone signals with a time-shared triple-resonance experiment, J. Biomol. NMR 33 (2005) 187–196.
[68] T. Parella, P. Nolis, Time-shared NMR experiments, Concepts Magn. Reson. Part A 36A (2010) 1–23.
[69] J.M. Lamley, J.R. Lewandowski, Simultaneous acquisition of homonuclear and heteronuclear long-distance contacts with time-shared third spin assisted recoupling, J. Magn. Reson. 218 (2012) 30–34.
[70] B.B. Das, S.J. Opella, Simultaneous cross polarization to (13)C and (15)N with (1)H detection at 60kHz MAS solid-state NMR, J. Magn. Reson. 262 (2016) 20–26.
[71] A.B. Nielsen, K. Szekely, J. Gath, M. Ernst, N.C. Nielsen, B.H. Meier, Simultaneous acquisition of PAR and PAIN spectra, J. Biomol. NMR 52 (2012) 283–288.
[72] R. Linser, B. Bardiaux, V. Higman, U. Fink, B. Reif, Structure calculation from unambiguous long-range amide and methyl 1H–1H distance restraints for a microcrystalline protein with MAS solid-state NMR spectroscopy, J. Am. Chem. Soc. 133 (2011) 5905–5912.
[73] T. Gopinath, G. Veglia, Dual acquisition magic-angle spinning solid-state NMR-spectroscopy: simultaneous acquisition of multidimensional spectra of biomacromolecules, Angew. Chem. Int. Ed. Engl. 51 (2012) 2731–2735.
[74] T. Gopinath, G. Veglia, Orphan spin operators enable the acquisition of multiple 2D and 3D magic angle spinning solid-state NMR spectra, J. Chem. Phys. 138 (2013) 184201.
[75] T. Gopinath, G. Veglia, Multiple acquisitions via sequential transfer of orphan spin polarization (MAeSTOSO): How far can we push residual spin polarization in solid-state NMR?, J Magn. Reson. 267 (2016) 1–8.
[76] T. Gopinath, G. Veglia, Experimental aspects of polarization optimized experiments (POE) for magic angle spinning solid-state NMR of microcrystalline and membrane-bound proteins, Methods Mol. Biol. 1688 (2018) 37–53.
[77] K. Sharma, P.K. Madhu, K.R. Mote, A suite of pulse sequences based on multiple sequential acquisitions at one and two radiofrequency channels for solid-state magic-angle spinning NMR studies of proteins, J. Biomol. NMR 65 (2016) 127–141.
[78] A. Viegas, T. Viennet, T.Y. Yu, F. Schumann, W. Bermel, G. Wagner, M. Etzkorn, UTOPIA NMR: activating unexploited magnetization using interleaved low-gamma detection, J. Biomol. NMR 64 (2016) 9–15.
[79] R. Bhattacharyya, L. Frydman, Ultrafast solid-state 2D NMR experiments via orientational encoding, J. Am. Chem. Soc. 128 (2006) 16014–16015.
[80] M. Gal, C. Melian, D.E. Demco, B. Blümich, L. Frydman, Solid-state single-scan 2D NMR under magic-angle-spinning, Chem. Phys. Lett. 459 (2008) 188–193.

[81] C. Oster, S. Kosol, C. Hartlmuller, J.M. Lamley, D. Iuga, A. Oss, M.L. Org, K. Vanatalu, A. Samoson, T. Madl, J.R. Lewandowski, Characterization of protein-protein interfaces in large complexes by solid-state NMR solvent paramagnetic relaxation enhancements, J. Am. Chem. Soc. 139 (2017) 12165–12174.
[82] R. Linser, B. Bardiaux, L.B. Andreas, S.G. Hyberts, V.K. Morris, G. Pintacuda, M. Sunde, A.H. Kwan, G. Wagner, Solid-state NMR structure determination from diagonal-compensated, sparsely nonuniform-sampled 4D proton-proton restraints, J. Am. Chem. Soc. 136 (2014) 11002–11010.
[83] M. Zinke, P. Fricke, C. Samson, S. Hwang, J.S. Wall, S. Lange, S. Zinn-Justin, A. Lange, Bacteriophage tail-tube assembly studied by proton-detected 4D solid-state NMR, Angew. Chem. Int. Ed. Engl. 56 (2017) 9497–9501.
[84] E. Kupce, K.R. Mote, P.K. Madhu, Experiments with direct detection of multiple FIDs, J. Magn. Reson. 304 (2019) 16–34.
[85] Y.T. van den Hoogen, S.J. Treurniet, H.C.P.F. Roelen, E. de Vroom, G.A. van der Marel, J.H. van Boom, C. Altona, Conformational analysis of the tetranucleotides m62A–m62A-U-m62A m62A =N6-dimethyladenosine) and U-m62A-U-m62A and of the hybrid dA-r(U-A), Eur. J. Biochem. 171 (1988) 155–162.
[86] D.S. Wishart, C.G. Bigam, J. Yao, F. Abildgaard, H.J. Dyson, E. Oldfield, J.L. Markley, B.D. Sykes, ^{1}H, ^{13}C and ^{15}N chemical shift referencing in biomolecular NMR, J. Biomol. NMR 6 (1995) 135–140.
[87] A.J. Shaka, J. Keeler, T. Frenkiel, R. Freeman, An improved sequence for broadband decoupling: WALTZ-16, J. Magn. Reson. 52 (1983) (1969) 335–338.
[88] D.H. Zhou, C.M. Rienstra, High-performance solvent suppression for proton detected solid-state NMR, J. Magn. Reson. 192 (2008) 167–172.
[89] L. Emsley, G. Bodenhausen, Gaussian pulse cascades: New analytical functions for rectangular selective inversion and in-phase excitation in NMR, Chem. Phys. Lett. 165 (1990) 469–476.
[90] D. Marion, M. Ikura, R. Tschudin, A. Bax, Rapid recording of 2D NMR spectra without phase cycling. Application to the study of hydrogen exchange in proteins, J. Magn. Reson. 85 (1989) (1969) 393–399.
[91] M. Baldus, A.T. Petkova, J. Herzfeld, R.G. Griffin, Cross polarization in the tilted frame: assignment and spectral simplification in heteronuclear spin systems, Mol. Phys. 95 (1998) 1197–1207.
[92] A.E. Bennett, R.G. Griffin, J.H. Ok, S. Vega, Chemical shift correlation spectroscopy in rotating solids: radio frequency-driven dipolar recoupling and longitudinal exchange, J. Chem. Phys. 96 (1992) 8624–8627.
[93] R. Verel, M. Ernst, B.H. Meier, Adiabatic dipolar recoupling in solid-state NMR: the DREAM scheme, J. Magn. Reson. 150 (2001) 81–99.
[94] E. Barbet-Massin, A.J. Pell, K. Jaudzems, W.T. Franks, J.S. Retel, S. Kotelovica, I. Akopjana, K. Tars, L. Emsley, H. Oschkinat, A. Lesage, G. Pintacuda, Out-and-back 13C–13C scalar transfers in protein resonance assignment by proton-detected solid-state NMR under ultra-fast MAS, J. Biomol. NMR 56 (2013) 379–386.
[95] J.R. Lewandowski, J. Sein, H.J. Sass, S. Grzesiek, M. Blackledge, L. Emsley, Measurement of site-specific ^{13}C spin-lattice relaxation in a crystalline protein, J. Am. Chem. Soc. 132 (2010) 8252–8254.
[96] I. Scholz, M. Huber, T. Manolikas, B.H. Meier, M. Ernst, MIRROR recoupling and its application to spin diffusion under fast magic-angle spinning, Chem. Phys. Lett. 460 (2008) 278–283.
[97] M. Ikura, L.E. Kay, A. Bax, A novel approach for sequential assignment of proton, carbon-13, and nitrogen-15 spectra of larger proteins: heteronuclear triple-resonance three-dimensional NMR spectroscopy. Application to calmodulin, Biochemistry 29 (1990) 4659–4667.
[98] L.E. Kay, M. Ikura, R. Tschudin, A. Bax, Three-dimensional triple-resonance NMR Spectroscopy of isotopically enriched proteins, J. Magn. Reson. 213 (2011) 423–441.
[99] A. Liu, R. Riek, G. Wider, C. von Schroetter, R. Zahn, K. Wuthrich, NMR experiments for resonance assignments of ^{13}C, ^{15}N doubly-labeled flexible polypeptides: application to the human prion protein hPrP(23–230), J. Biomol. NMR 16 (2000) 127–138.
[100] A.J. Shaka, C.J. Lee, A. Pines, Iterative schemes for bilinear operators; application to spin decoupling, J. Magn. Reson. 77 (1988) (1969) 274–293.
[101] S. Ciofi-Baffoni, A. Gallo, R. Muzzioli, M. Piccioli, The IR-(1)(5)N-HSQC-AP experiment: a new tool for NMR spectroscopy of paramagnetic molecules, J. Biomol. NMR 58 (2014) 123–128.
[102] M.J. Knight, I.C. Felli, R. Pierattelli, L. Emsley, G. Pintacuda, Magic angle spinning NMR of paramagnetic proteins, Acc. Chem. Res. 46 (2013) 2108–2116.